



# Scalable fabrication of high-performance graphene/polyamide 66 nanocomposites with controllable surface chemistry by melt compounding

Elcin Cakal Sarac<sup>1</sup> | Leila Haghighi Poudeh<sup>2</sup> | Ilayda Berktaş<sup>2</sup> |  
Burcu Saner Okan<sup>2</sup>

<sup>1</sup>Kordsa Teknik Tekstil A.S., Teknopark Istanbul, Istanbul, Pendik, Turkey

<sup>2</sup>Sabancı University Integrated Manufacturing Technologies Research and Application Center & Composite Technologies Center of Excellence, Teknopark Istanbul, Istanbul, Pendik, Turkey

## Correspondence

Burcu Saner Okan, Sabancı University Integrated Manufacturing Technologies Research and Application Center & Composite Technologies Center of Excellence, Teknopark Istanbul, Pendik, 34906, Istanbul, Turkey.  
Email: burcu.saner@sabanciuniv.edu

## Abstract

Scalable and ease fabrication of high-performance graphene reinforced polyamide 66 (PA66) nanocomposites by melt-mixing were achieved by selecting ideal graphene reinforcement having high C/O ratio. In this study, single-layer amine functionalized reduced graphene oxide and multi-layer thermally exfoliated graphene oxide (TEGO) were used to investigate the influence of surface chemistry and dispersion state on crystallization behaviors, mechanical, and thermal properties of graphene reinforced PA66 nanocomposites. Both types of graphenes acted as nucleating agent but TEGO showed the better performance due to its intercalated structure formation mechanism and efficient viscous flow during melting. Mechanical results indicated that 0.5 wt% TEGO based PA66 nanocomposite showed the highest tensile properties by increasing tensile modulus and tensile strength up to 45% and 16.1%, respectively. In addition, TEGO reinforced nanocomposites showed more stable viscoelastic behavior by reaching a plateau at high temperatures and restraining long-range motion of polymer chains.

## KEYWORDS

composites, graphene, manufacturing, mechanical properties, polyamides, structure-property relationships

## 1 | INTRODUCTION

Polyamides (PAs) are widely used engineering thermoplastics with various applications due to their high stiffness, toughness, and resistance to dynamic fatigue, high temperature, and chemical resistance.<sup>1–3</sup> However, poor thermal stability, low electrical conductivity, and high percent of shrinkage of PAs with growing market needs limit the use of polymers,<sup>4</sup> and thus, recent studies have been focused on the incorporation of nanofillers, such as, carbon based nanoparticles and nanoclay that meet the requirements of the market.<sup>5–8</sup> Among carbon based nanoparticles, there

has been a growing interest of using graphene and its derivatives such as graphene oxide (GO), graphene nanoplatelet (GNP) as reinforcements for the development of high performance PA66 based composites.<sup>9–12</sup> Herein, graphene with its high thermal, mechanical, and electrical properties along with high surface area seems a promising filler to attain an ideal composite structure.<sup>13–15</sup> In the case of GO, the lateral dimensions graphene sheets in polymer matrix<sup>16</sup> and poor binding affinity between polymer and graphene cause nonhomogeneous distribution and agglomeration in the polymer matrix<sup>17</sup> that directly affect the reinforcing efficiency.<sup>10</sup>

The interfacial interactions between polymer and graphene play an important role in order to reveal the exceptional properties of graphene in composites since the strengthening mechanism of carbon-based nanofiller in matrix is fully realized by the successful bonding of the two materials to each other.<sup>18</sup> There are various studies about the integration of graphene in polyamide matrix in the literature. For instance, Yesildag et al improved the Young's modulus up to 20% and tensile strength of the matrix up to 15% compared with neat PA6 by incorporating 1 wt% polar graphene into PA6 by using a co-rotating intermeshing twin screw extruder but also stated that the Young's modulus did not increase with increasing graphene content due to the agglomeration of graphene.<sup>19</sup> Furthermore, Xu and Gao enhanced the tensile strength and Young's modulus of PA6 composites by 2.1 and 2.4 folds, respectively, by the addition of 0.1% graphene by in situ ring-opening polymerization of PA6.<sup>20</sup>

In addition to the direct usage of neat graphene materials, surface functionalization has been carried out to make proper interactions with the selected matrix. Hou and coworkers reported the preparation of PA6 and amine functionalized GO by in situ ring-opening polymerization of caprolactam resulting in ease dispersion of GO sheets in organic compounds.<sup>21</sup> In another work, Gong et al provided uniform dispersion with ester functionalized GO sheets in PA6 matrix by enhancing the interface adhesion between nanosheets and matrix.<sup>22</sup> Furthermore, Steurer et al introduced 10 wt% of thermally reduced graphite oxide into PA6 by twin-screw extruder and increased Young's modulus of PA6 from 1650 to 2430 MPa.<sup>23</sup> While PA66 has better mechanical performance and abrasive resistance<sup>24,25</sup> compared with PA6, neat PA66 still requires the modification to meet the demand in the emerging thermoplastic market. In addition, weak interfacial interactions between GO and PA66, and poor dispersion during in-situ polymerization, and melt blending processes seem the bottlenecks in the industrialization of PA66 based nanocomposites.

Although significant advances have been made in the utilization of graphene materials in PA based matrices, there is no report that investigates the effect of surface chemistry of graphene with the controlled C/O ratio on the crystallinity and mechanical and thermal behaviors of PA66 based compounds. Understanding of chemical exfoliation and thermal expansion, the steps for the fabrication of GO and rGO, can provide to elaborate the relationship between the reinforcement and the selected polymer matrix. Therefore, the aim of this study is to (a) conduct a comprehensive comparison of two different types of graphenes, which are thermally exfoliated graphene oxide (TEGO) and amine functionalized reduced graphene oxide (rGO) and (b) establish a feasible

approach for the production of high performance PA66 nanocomposites by tailoring their crystallization behavior, mechanical, and thermal properties and viscosity profiles. The effect of different functional groups of single layer rGO with terminal amino ends and multi-layer TEGO having high carbon functional groups on the characteristics of PA66 were investigated in a systematic manner by spectroscopic techniques. In addition to the detailed surface chemistry analysis, the influence of graphene layer number on the performance of PA66 during melt mixing was investigated to understand the ideal composition in graphene intercalated composite structure.

## 2 | EXPERIMENTAL

### 2.1 | Materials

The following materials were used in experiments: PA66 polymer (Zytel E51HSB NC010, Dupont), thermally exfoliated graphene oxide (TEGO, NANOGRAFEN Co.) produced by oxidation and thermal expansion steps, graphite flakes (+100 mesh size, Sigma-Aldrich), hydrazine hydrate (N<sub>2</sub>H<sub>4</sub>, 50%–60%, Sigma-Aldrich), hydrogen peroxide (30% H<sub>2</sub>O<sub>2</sub>, Sigma-Aldrich), and potassium permanganate (KMnO<sub>4</sub>, Merck & Co.).

### 2.2 | Synthesis of reduced graphene oxide (rGO)

Graphene oxide (GO) was synthesized through improved Hummers' method.<sup>26,27</sup> In GO synthesis, graphite flakes were mixed with the concentrated H<sub>2</sub>SO<sub>4</sub>/H<sub>3</sub>PO<sub>4</sub> (v: v = 9:1) in the presence of KMnO<sub>4</sub> as an oxidizing agent for 1 day at 50°C. Then, the mixture was poured on the ice bath having 3 ml of H<sub>2</sub>O<sub>2</sub>, and filtration and centrifugation processes were applied to separate GO sheets and remove the unreacted parts. Chemical reduction was carried out by hydrazine hydrate (the weight ratio of hydrazine hydrate/GO = 1) as a reducing agent through refluxing about 3 h. At the final step, reduced graphene oxide (rGO) powder was immoderately isolated by filtration, and washed with distilled water for several times, then dried at 60°C for 24 h to remove residual solvent.

### 2.3 | Fabrication of graphene reinforced PA66 nanocomposites

For the fabrication of graphene reinforced PA66 nanocomposites, TEGO, and rGO were dispersed into PA66 matrix at 300°C and 4700 rpm by using custom-made

Gelimat Thermokinetic Mixer. The contents of rGO and TEGO in the nanocomposites were adjusted in the range between 0.25 and 1 wt% to attain an optimum amount and prevent the agglomeration of graphene sheets. After mixing process, samples were used in injection molding process to prepare composite specimens for mechanical tests.

## 2.4 | Characterization

Surface morphologies of graphene samples and cross-sections of composite specimens were investigated by Leo Supra 35VP Field Emission Scanning Electron Microscope (SEM). The surface areas of graphene samples were measured by the Quantachrome NOVA 2200e series Surface Analyzer. The samples' crystallinity was examined by Bruker X-ray diffraction (XRD) with a  $\text{CuK}\alpha$  radiation source. The number of graphene layers in multi-layered structures was calculated by Debye–Scherrer equation (Equation 1) as follows:

$$t = 0.89\lambda / \beta \cos\theta$$

$$n = t/d \quad (1)$$

where  $t$  is thickness,  $\beta$  is full width at half maximum, and  $d$  is interlayer spacing obtained from XRD patterns, and  $n$  is layer number. The structural properties of graphene samples were characterized by Renishaw Raman spectroscopy (UK) with the laser wavelength of 532 nm. The surface functional groups of samples were studied by Thermo Scientific Fourier Transform Infrared Spectroscopy (FTIR, Germany) and Thermo Scientific K-Alpha X-ray Photoelectron Spectrometer (XPS, Germany). Thermal behaviors of composite specimens were investigated by Mettler Toledo differential scanning calorimeter (DSC) under  $\text{N}_2$  atmosphere. Tensile and flexural properties of composite specimens were investigated by using the Instron 5982 Static Test Machine with a 5 kN load cell. Rheological characterization of graphene reinforced composite samples was performed by using MCR 702 TwinDrive Anton Paar Rheometer (Austria).

## 3 | RESULTS AND DISCUSSION

### 3.1 | The characteristic properties of rGO and TEGO

It is well known that the performance of graphene-based composites strongly depends on the variety and content of functional groups present on the edge and basal plane of graphene.<sup>28</sup> Thermal and chemical modifications

increase the carbon/oxygen ratio of graphene, which greatly affects the dispersion state of graphene in polymeric matrix.<sup>29</sup> In the present study, two different graphene types were selected to monitor the effect of layer number and surface oxygen and nitrogen functional groups on the performance of PA66 based nanocomposites. Figure 1(a) shows the SEM image of rGO with smooth layers of graphene. In contrast, TEGO has the accordion-like morphology indicating the separation of GO layers during thermal treatment as seen in Figure 1(b). BET surface areas of TEGO and rGO are  $11 \text{ m/g}^2$  and  $483 \text{ m/g}^2$  respectively.

XRD and Raman spectroscopy are efficient characterization tools in order to understand the differences in the layer number of each graphene sample. Figure 2(a) exhibits XRD patterns of TEGO and rGO which both of them have the (002) characteristic graphitic peak. However, the position of this peak in rGO slightly shifted toward lower angles and became broaden since the chemical reduction by hydrazine causes the complete restoration of the aromatic carbon  $\text{sp}^2$  lattice spacing<sup>30</sup> when compared with XRD pattern of GO given in Figure S1a. On the other hand, TEGO has graphitic peak supporting its multi-layered structure and the number of graphene layers in TEGO was calculated as 25 based on (002) peak by using Debye–Scherrer equation. Furthermore, Raman spectroscopy analysis was carried out to further understand the defects and disorders in each graphene. The Raman spectrum of TEGO has three main characteristic peaks of graphene having D, G, and 2D bands are seen at 1355, 1582, and 2721  $\text{cm}^{-1}$ , respectively, in Figure 2(b). The intensity of D band indicates the disorderness and defects in the structure whereas G band attributes to the vibrational mode of carbon  $\text{sp}^2$  crystallites.<sup>31,32</sup> The intensity ratio of D/G ( $I_D/I_G$ ) is a relative analysis tool to quantify the defects in the graphitic structures.<sup>33</sup> According to Figure 2,  $I_D/I_G$  ratio of rGO was calculated as 1.15, which is much higher than that of TEGO (0.26). This difference stems from the destruction of graphene planes by breaking down a large amount of  $\text{sp}^2$  carbon atoms during the chemical reduction of GO. The details about Raman peak intensities and peak ratios are given in Table S1 in the supplementary document.

Chemical composition has a significant influence on the interfacial interactions between polymer chains and reinforcement. Therefore, surface functional groups of rGO and TEGO were investigated to understand their dispersion behavior in PA66 matrix. Regarding XPS analyses of rGO and TEGO given in Table 1 and Figure 3, TEGO and rGO contain 2 and 20.4 at% oxygen, respectively. In the C1s XPS spectrum of TEGO, C=C bonds with large intensity implied the  $\text{sp}^2$  arrangement of hexagonal rings of six carbons in the structure (Table S2). On the other

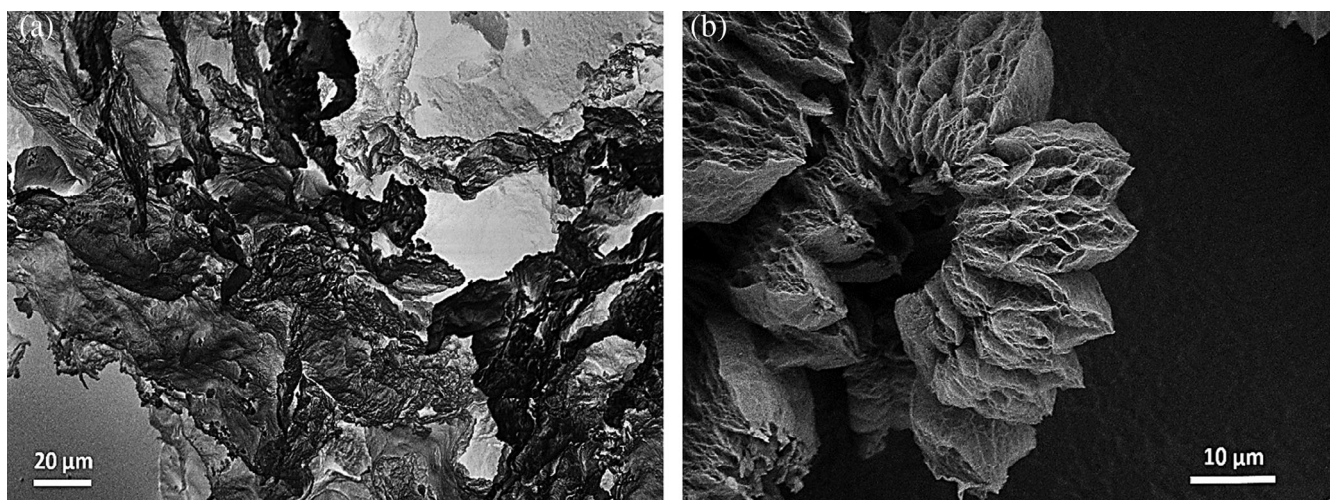


**FIGURE 1** SEM images of (a) rGO and (b) TEGO

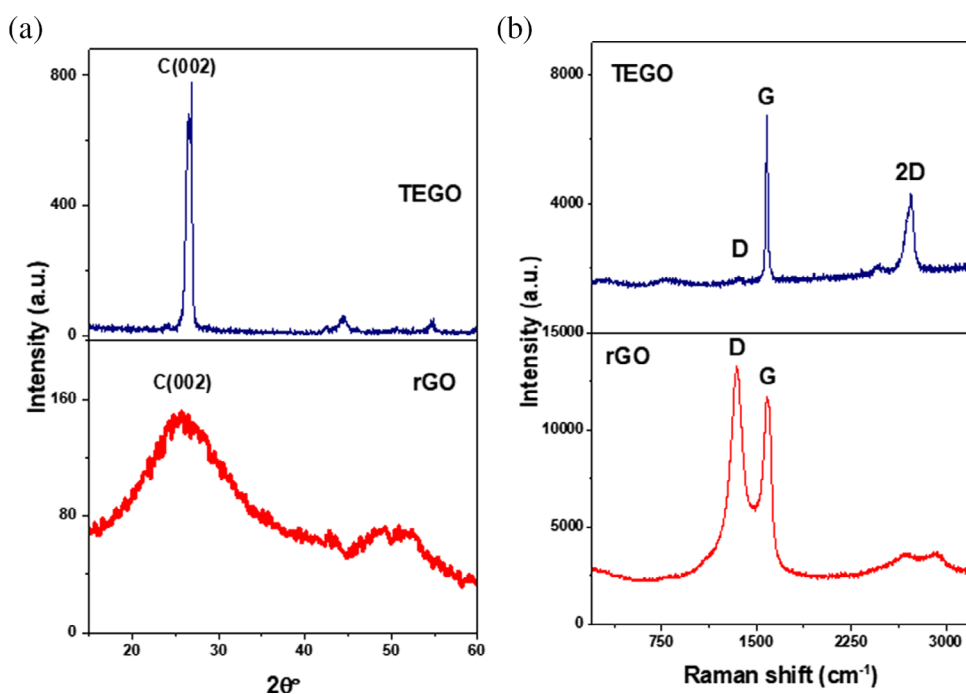


**FIGURE 2** (a) XRD patterns and (b) Raman spectra of rGO and TEGO [Color figure can be viewed at [wileyonlinelibrary.com](http://wileyonlinelibrary.com)]

**TABLE 1** XPS results of rGO and TEGO

| Samples | C (at%) | O (at%) | N (at%) |
|---------|---------|---------|---------|
| rGO     | 74.1    | 20.4    | 5.5     |
| TEGO    | 98.0    | 2.1     | —       |

hand, the presence of nitrogen in the XPS survey of rGO indicated the covalent attachment of amine group of hydrazine hydrate to GO during the reduction process.<sup>34</sup> In conclusion, TEGO has high carbon content and comparably lower amount of oxygen when compared with rGO.

### 3.2 | Mechanical properties of rGO and TEGO based PA66 nanocomposites

In order to observe the effect of graphene layer number and surface functional groups and get an ideal graphene amount in PA66 nanocomposites, three different graphene ratios of 0.25, 0.5, and 1 wt% were adjusted for dispersion process by high shear thermokinetic mixer. Figure 4 exhibits stress–strain curves of neat PA66 and its nanocomposites obtained from tensile and flexural tests. In tensile tests, the best results from the integration of rGO in PA66 were obtained with 0.25 wt% additive loading, and tensile modulus and strength increased up to

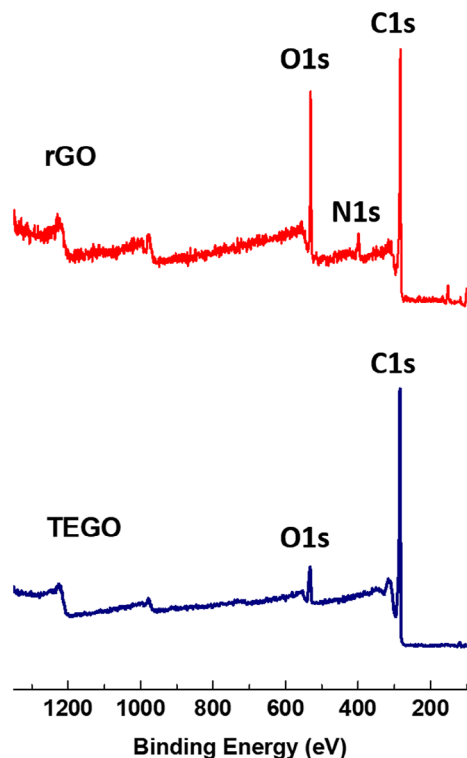


**FIGURE 3** XPS survey scan spectra of rGO and thermally exfoliated graphene oxide [Color figure can be viewed at [wileyonlinelibrary.com](http://wileyonlinelibrary.com)]

10% and 5.2%, respectively. However, there is no big difference in mechanical properties of 0.25 and 0.5 wt% rGO reinforced PA66 nanocomposites as shown in Tables 2 and 3. In terms of TEGO, the loading amount of 0.5 wt% provided significant improvement in tensile modulus and strength values, which were improved about 45% and 16.1%, respectively. On the other hand, maximum improvement in flexural properties of TEGO based nanocomposites was attained by the addition of 1 wt% nanofiller since the enhancement in flexural strength indicates the better dispersion of graphene sheets resulting in the reduction in stress concentrations in composite structure.<sup>29</sup> In rGO based nanocomposites, amino based functional groups on the surface of graphene causes covalent interactions with polymer chains during melt compounding process. Hence, this prevents the role of additive as a reinforcement in the matrix and thus does not allow efficient stress transfer at high applied loads when compared with TEGO reinforced nanocomposites.<sup>35,36</sup>

In Table 2, the values of tensile strain at break of composites by incorporating graphene reinforcements were decreased since graphene leads to a decrease in ductility resulting in an increase in brittleness of composites and thus the formation of fractures in TEGO and rGO based composites before deforming much under a tensile load of neat PA 66.<sup>37</sup>

Furthermore, it is well known that the dispersion state of graphene in the matrix greatly affects the mechanical performance of graphene based polymeric composites. Covalent functionalization between graphene and polymer matrix leads to the disruption of the  $sp^2$ -hybridized network whereas noncovalent interactions of weak  $CH - \pi$  and/or  $\pi - \pi$  provide to control interfacial interactions between matrix and reinforcement.<sup>29</sup> During melt compounding, the external forces generated by viscous flow have ability to separate the weak agglomerated graphene sheets.<sup>35,38</sup> However, the addition of rGO having high surface area resulted in a system with low viscosity matrix when compared with that of TEGO. Therefore, the viscous forces were insufficient to break down the tight rGO agglomerates and aggregates. The strongly associated agglomerates in the rGO-PA66 composites and inefficiency of viscous flow matrix resulted in a low improvement in the tensile modulus of PA66 in comparison of TEGO based nanocomposites.

### 3.3 | Crystallization effect of rGO and TEGO on PA66 nanocomposites

The presence of a foreign substrate in the microstructure of a melt semicrystalline polymer initiates the nucleation of crystalline phases, as a result of an increased surface energy at their interface. Therefore, the integration of graphene as a nanofiller into the PA66 matrix brings about the enhancement in the crystallization of nanocomposites.<sup>39</sup> Figure 5 represents XRD patterns of PA66 nanocomposites having 0.5 wt% rGO and 0.5 wt% TEGO. In the diffraction pattern of PA66, the broad XRD peak at around  $2\theta = 21^\circ$  attributes to the inter-chain hydrogen bonded (100) plane of amide groups of PA66.<sup>40</sup> This peak has small shoulder at around  $2\theta = 23^\circ$  indicating the overlapping diffraction peaks for (010) and (110) planes of PA66.<sup>40</sup> After the integration of TEGO or rGO in PA66, the peak intensity of (100) was decreased and the peak of (010/110) became more distinguishable due to the changes in d-spacing of intersheets.<sup>41</sup> It should be noted that the position of (100) peak in TEGO-based nanocomposites was shifted toward lower  $2\theta$  values when compared with the neat and GO-based PA66s. The reason behind this change lies in the accordion-like morphology of TEGO, which leads to higher interlayer spacing of PA66. Moreover, graphene sheets with high aspect ratio could easily penetrate through polyamide chains resulting in the appearance of a broad and comparably intense peak of kinetically favored  $\gamma(002)$  phase at around  $2\theta = 10^\circ$ .<sup>42</sup> In case of rGO, the intensity of  $\gamma(002)$  is slightly higher owing to the nature of its structure,

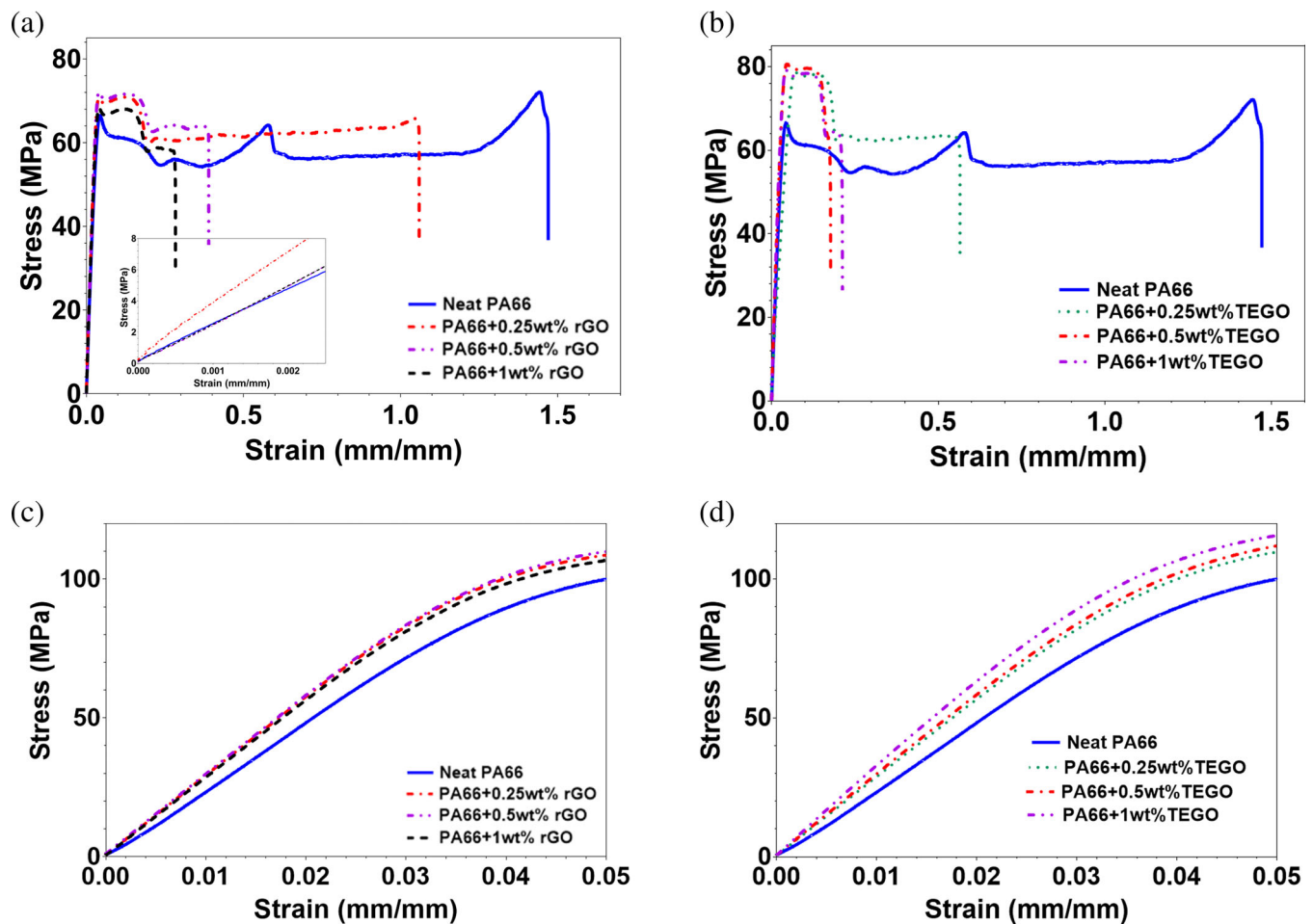


**FIGURE 4** (a, b) tensile stress–strain curves and (c, d) flexural stress–strain curves of nanocomposites by different reinforcement loadings [Color figure can be viewed at [wileyonlinelibrary.com](http://wileyonlinelibrary.com)]

**TABLE 2** Tensile properties and their improvement percentages of PA66 nanocomposites reinforced by rGO and TEGO

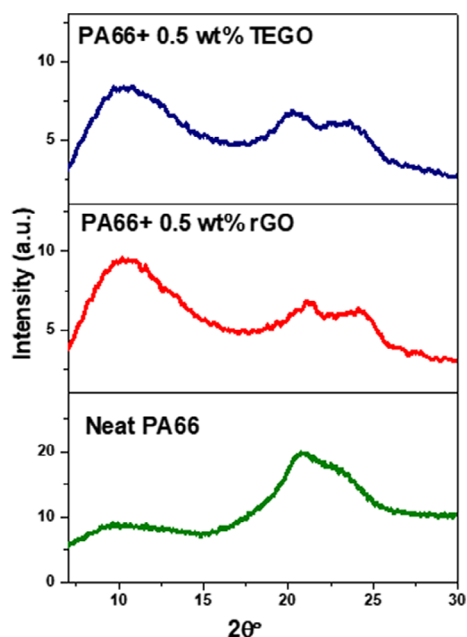
| Specimens            | Tensile modulus (MPa) | Tensile modulus improvement (%) | Tensile strength (MPa) | Tensile strength improvement (%) | Tensile strain at break (%) |
|----------------------|-----------------------|---------------------------------|------------------------|----------------------------------|-----------------------------|
| Neat PA66            | 2400                  | —                               | 69.8                   | —                                | 150                         |
| PA66 + 0.25 wt% rGO  | 2647                  | 10                              | 73.5                   | 5.2                              | 110                         |
| PA66 + 0.5 wt% rGO   | 2587                  | 8                               | 71.8                   | 2.9                              | 39                          |
| PA66 + 1 wt% rGO     | 2614                  | 9                               | 70.4                   | 0.9                              | 28                          |
| PA66 + 0.25 wt% TEGO | 3195                  | 33                              | 78.7                   | 12.8                             | 94                          |
| PA66 + 0.5 wt% TEGO  | 3473                  | 45                              | 81.0                   | 16.1                             | 21                          |
| PA66 + 1 wt% TEGO    | 2984                  | 24                              | 79.0                   | 13.2                             | 16                          |

which has single graphene sheets.<sup>31</sup> This led to the formation of exfoliated structure. On the other hand, TEGO has multi-layer structure which promotes the generation of the intercalated structures.<sup>27,28</sup> In addition, Table 4 provides crystallinity index values of 0.5 wt% loaded PA66 nanocomposites. The results showed that rGO has

slightly higher crystallinity than TEGO, but both these reinforcements acted as nucleation agents in compounding process. Therefore, the differences in the dispersion states of rGO and TEGO affected the mechanical performance of nanocomposites as previously discussed in the previous section. The results indicated that

**TABLE 3** Flexural properties and their improvement percentages of PA66 nanocomposites reinforced by rGO and TEGO

| Specimens            | Chord modulus (MPa) | Flexural modulus improvement (%) | Flexural strength (MPa) | Flexural strength improvement (%) |
|----------------------|---------------------|----------------------------------|-------------------------|-----------------------------------|
| Neat PA66            | 2570                | —                                | 102                     | —                                 |
| PA66 + 0.25 wt% rGO  | 2878                | 12.0                             | 111                     | 8.8                               |
| PA66 + 0.5 wt% rGO   | 2885                | 12.3                             | 113                     | 10.8                              |
| PA66 + 1 wt% rGO     | 2810                | 9.3                              | 109                     | 6.9                               |
| PA66 + 0.25 wt% TEGO | 2833                | 10                               | 110                     | 7.8                               |
| PA66 + 0.5 wt% TEGO  | 2898                | 13                               | 110                     | 7.8                               |
| PA66 + 1 wt% TEGO    | 2996                | 17                               | 118                     | 15.7                              |

**FIGURE 5** X-ray diffraction patterns of PA66 composites having 0.5 wt% rGO and 0.5 wt% TEGO [Color figure can be viewed at wileyonlinelibrary.com]

intercalated structure formed by TEGO provided better improvement in mechanical strength in PA66 matrix in comparison of rGO based nanocomposites.

The influence of two types of nano additives on the crystallinity of PA66 nanocomposites was also examined by FTIR shown in Figure 6 and Figure S3. Pristine PA66 and 0.5 rGO and 0.5 wt% TEGO reinforced nanocomposites have two temperature-dependent crystalline peaks at 934 and 1198  $\text{cm}^{-1}$  while the peak at 1630  $\text{cm}^{-1}$  is temperature-independent and considered as the reference peak.<sup>44,45</sup> The transmittance ratio of these dependent and independent bands ( $T_{1198}/T_{1630}$ ) provides the changes in the crystallinity of nanocomposites as given in Table 5. These results indicated that the

**TABLE 4** Crystallinity index of 0.5 wt% loaded PA66 nanocomposites

| Crystallinity index | Crystallinity (%) | Amorphous (%) |
|---------------------|-------------------|---------------|
| Neat PA66           | 34.1              | 65.9          |
| PA66 + 0.5 wt% TEGO | 35.9              | 64.1          |
| PA66 + 0.5 wt% rGO  | 37.2              | 62.8          |

incorporation of rGO and TEGO into the PA66 matrix enhanced the crystallinity, which was also verified by XRD characterization.

For the detailed investigation of nucleation effect, DSC analysis was applied to analyze the crystalline behavior of PA66 nanocomposites. Table 6 summarizes DSC results of neat PA66 and 0.5 wt% graphene based PA66 nanocomposites. There is no notable difference in melting temperature of the fabricated nanocomposites. However, there are variations in the percent crystallinity, which is calculated by using the equation as follows:

$$X_c = \left( \frac{\Delta H_m}{\Delta H_m^{100\%}} \right) \times 100\% \quad (2)$$

where  $X_c$  is the degree of crystallinity,  $\Delta H_m$  is enthalpy of melting, and  $\Delta H_m^{100\%}$  is enthalpy of purely crystalline (J/g).  $\Delta H_m^{100\%}$  is a reference for neat crystalline PA66 as about 188.4 J/g.<sup>46</sup> There was a sharp increase in  $X_c$  values by the addition of each type of graphene additive. However, as the amount of graphene increased, the strong interactions between the graphene sheets and matrix led to the reduction in the polymeric chain mobility and thus hindered the crystal growth.<sup>47</sup> In case of TEGO, the smaller reduction rate in crystallinity could be attributed to the multi-layer structure of TEGO and the absence of amine groups since the amine functional groups terminates the polymeric chains of PA66 and thus led to a sharp decrease in the crystallinity.<sup>21,48</sup> Considering

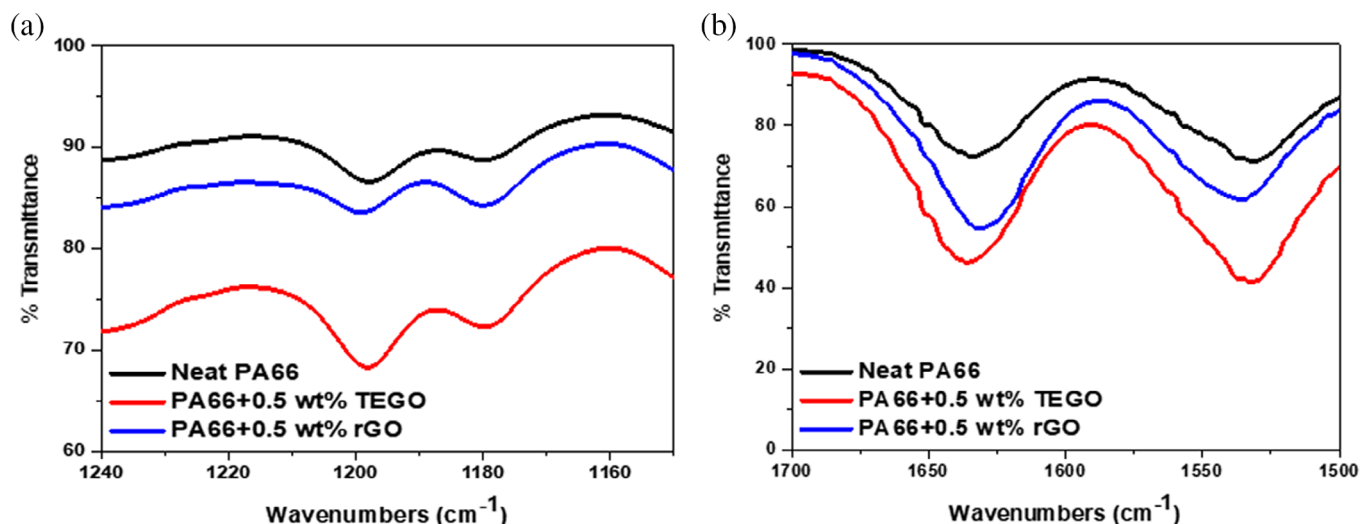


**FIGURE 6** Fourier Transform Infrared Spectroscopy spectra of (a) crystalline band and (b) C=O stretching vibration modes of neat PA66 and nanocomposites [Color figure can be viewed at [wileyonlinelibrary.com](http://wileyonlinelibrary.com)]

**TABLE 5** The intensity values of crystalline and reference peaks and their ratios

| Samples              | $T_{1198}$ (a.u.) | $T_{1630}$ (a.u.) | $T_{1198/1630}$ |
|----------------------|-------------------|-------------------|-----------------|
| Neat PA66            | 86.6              | 72.2              | 1.20            |
| PA66 + 0.25 wt% rGO  | 72.1              | 27.3              | 2.64            |
| PA66 + 0.5 wt% rGO   | 83.6              | 54.8              | 1.53            |
| PA66 + 1 wt% rGO     | 85.9              | 62.7              | 1.37            |
| PA66 + 0.25 wt% TEGO | 71.6              | 44.1              | 1.62            |
| PA66 + 0.5 wt% TEGO  | 68.3              | 46.4              | 1.47            |
| PA66 + 1 wt% TEGO    | 77.4              | 60.8              | 1.27            |

**TABLE 6** Melting temperatures and crystallinity index values of pristine PA66 and its nanocomposites

| Samples              | $T_m$ (°C) | $\Delta H_m$ (J/gr) | $X_c$ (%) |
|----------------------|------------|---------------------|-----------|
| Neat PA66            | 262        | 48.2                | 25.6      |
| PA66 + 0.25 wt% rGO  | 263        | 70.5                | 46.4      |
| PA66 + 0.5 wt% rGO   | 263        | 70.4                | 46.2      |
| PA66 + 1 wt% rGO     | 263        | 68.5                | 42.8      |
| PA66 + 0.25 wt% TEGO | 261        | 76.9                | 40.6      |
| PA66 + 0.5 wt% TEGO  | 261        | 76.0                | 40.3      |
| PA66 + 1 wt% TEGO    | 261        | 74.7                | 39.7      |

both XRD and DSC results, increasing nanofiller content reduces the crystallinity of composites.<sup>21</sup> DSC curves of PA66 nanocomposites with different rGO and TEGO loadings are given in Figure S2a and b in supporting

document, respectively. Crystallinity index of rGO based nanocomposites have slightly higher values in comparison of TEGO reinforced ones. An increase in TEGO concentration did not change the crystallinity index values significantly. This might come from the multi-layered structure of TEGO and their alignment in polymer matrix. On the other hand, there is a slight difference in 0.25 and 0.5 wt% rGO loadings, but a decrease in crystallinity is observed as rGO content increases. This might stem from the aggregation of rGO layers and the formation of crosslinks between amine groups of rGO and PA66.<sup>2</sup>

### 3.4 | Rheological behaviors of rGO and TEGO based PA66 nanocomposites

The steady shear viscosity is an important parameter to estimate the processability of composites and this data

are obtained from the complex viscosity ( $\eta^*$ ).<sup>49</sup> The change in the viscosity by the addition of graphene directly affects storage modulus ( $G'$ ) of the composite.<sup>50</sup> Figure 7 compares rheological properties of rGO and TEGO based PA66 nanocomposites in terms of  $G'$  and  $\eta^*$  as a function of time and temperature by three different graphene loadings. When compared with the changes of  $\eta^*$  as a function of time in terms of rGO based nanocomposites, the viscosity values of neat and rGO based samples decrease as time increases at the melting stage but after a while, the viscosity of all rGO based samples has been started to become stable. Herein, reaching the plateau in the viscosity curves means the restraints of the long-range motion of PA66 macromolecular chains.<sup>51</sup> The same behavior was also detected in the viscosity behaviors of TEGO based

nanocomposites as seen in Figure 7(b). Especially 1 wt % TEGO reinforced PA66 specimen showed more stable viscoelastic behavior and a plateau at high temperatures indicating the existence of percolation of graphene particles and the formation of interconnected graphene network.

Storage modulus indicates the elastic portion of the viscoelastic behavior in the composite specimens and the stored deformation energy. Figure 7(c) and (d) show the storage modulus of rGO and TEGO based nanocomposites at different loadings as a function of the temperature. In rGO nanocomposites, as rGO content increases, storage modulus decreases whereas the curves become linear by increasing temperature meaning typical fluid behavior. On the other hand, the rheological behaviors of TEGO reinforced nanocomposites

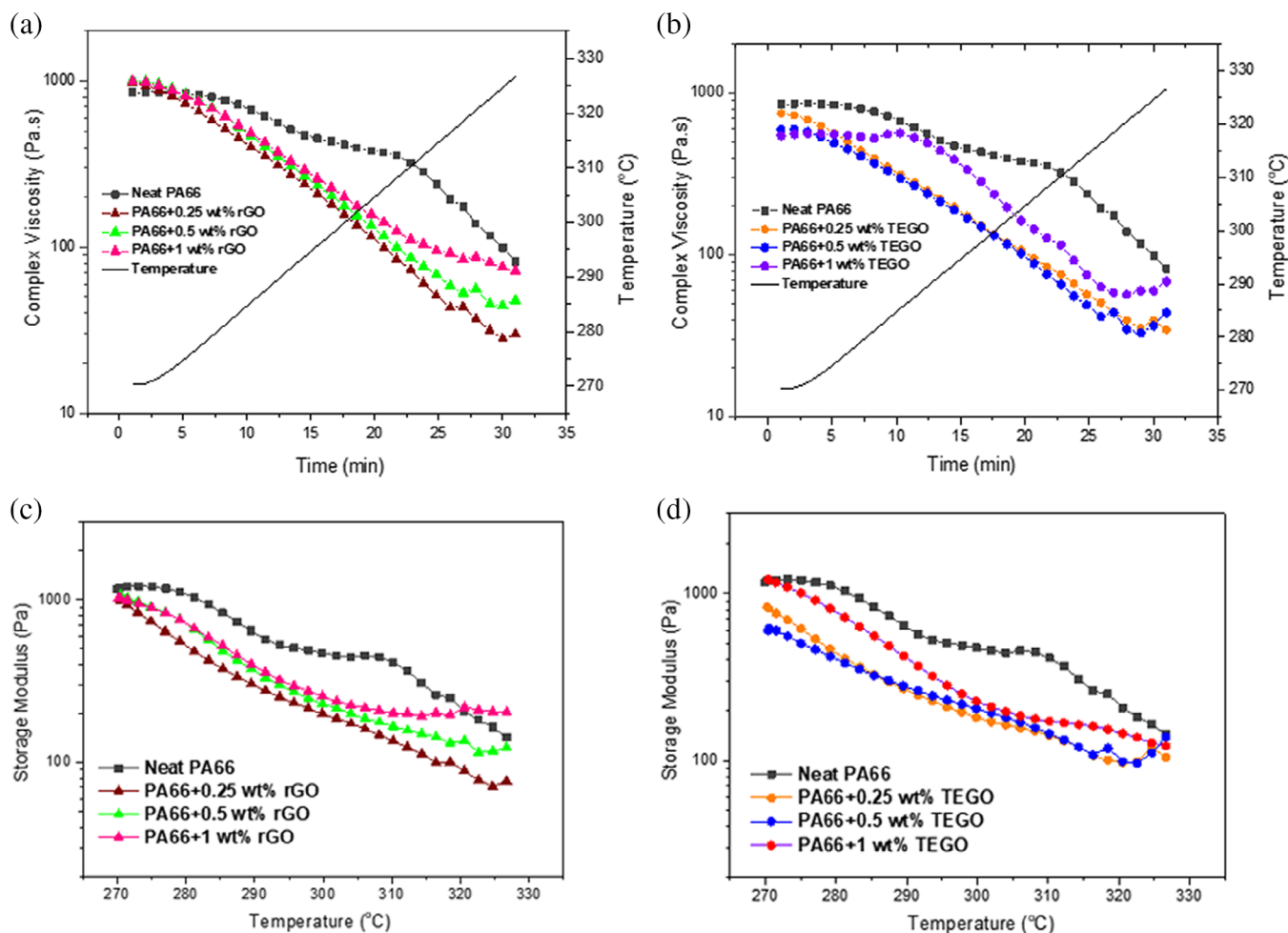


**FIGURE 7** Complex viscosity of (a) neat PA66 and rGO loaded nanocomposites, (b) neat PA66 and TEGO loaded nanocomposites as a function of temperature and time, and storage modulus of (c) neat PA66 and rGO loaded nanocomposites, (d) neat PA66 and TEGO loaded nanocomposites as a function of temperature [Color figure can be viewed at [wileyonlinelibrary.com](http://wileyonlinelibrary.com)]

showed that there was a linear decrease in their storage modulus as a function of temperature and also the samples showed stable plateau at high temperatures.

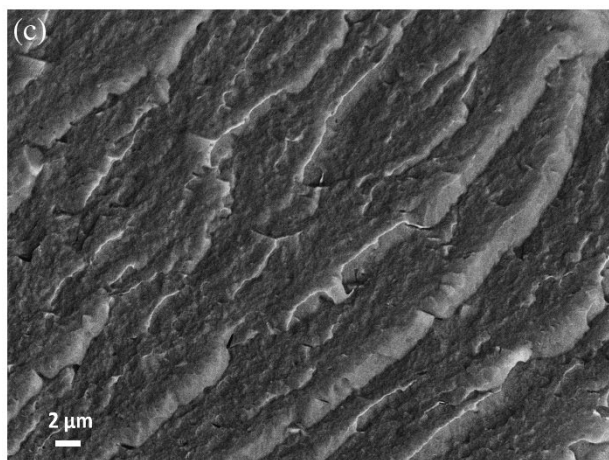
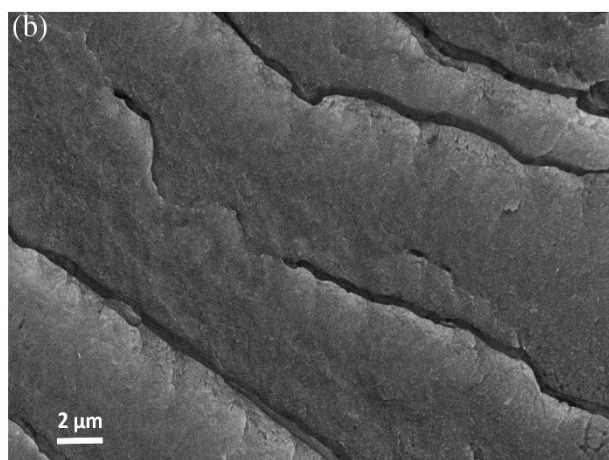
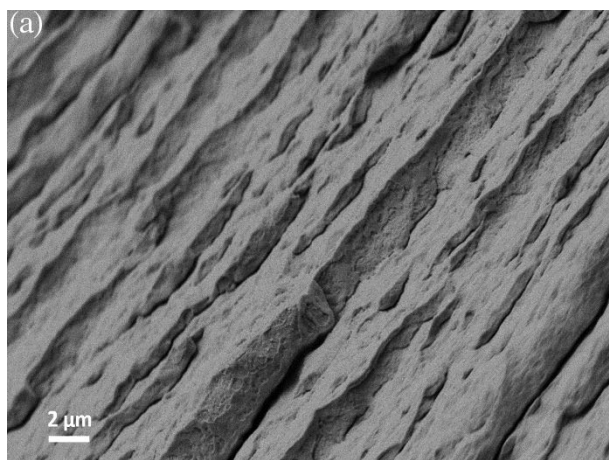


**FIGURE 8** Scanning electron microscope images of (a) neat PA66, (b) PA66 + 0.5 wt% rGO, and (c) PA66 + 0.5 wt% TEGO

### 3.5 | Morphological differences in cross-sections of graphene reinforced PA66 nanocomposites

In order to understand the dispersion quality of graphene sheets in the PA66 matrix, the morphological differences of freeze-fracture surfaces of neat PA66, rGO, and TEGO reinforced nanocomposites were analyzed by SEM. As shown in Figure 8(a), pristine PA66 has fragmented structure and the freeze-fracture surface of composite became smoother, and roughness was significantly reduced after the dispersion of single-layer rGO as shown in Figure 8(b). In case of multi-layer TEGO, which has worm-like structure, the surface roughness of nanocomposites was increased as seen in Figure 8(c).

## 4 | CONCLUSIONS

In summary, graphene sheets with different C/O ratio and layer number were distributed in PA66 matrix in order to prepare mechanically improved nanocomposites by tailoring crystallization and rheological behaviors. TEGO with high C/O ratio and multi-layered structure showed better mechanical improvement in PA66 based composites in comparison of rGO since the oxygen contents of TEGO and rGO obtained from XPS characterization are between 2 at% and 20.4 at%, respectively. Strong interfacial interactions were achieved with TEGO based nanocomposites owing to its intercalated structure formation. Therefore, the significant improvement in tensile modulus and strength was observed for 0.5 wt% TEGO reinforced PA66 nanocomposites. On the other hand, single sheet rGO did not impart convincing mechanical enhancement due to the presence of amino functional groups that might lead to covalent interaction with the polymer backbone of PA66 and thus the reduction in the efficiency of reinforcing capability. In other words, the high oxygen content in rGO led to the disruption of the  $\pi$ -conjugated system and thus resulting in the performance loss of PA66 based nanocomposites. In addition, crystallization behavior of graphene based PA66 nanocomposites carried out by DSC and the thermal behavior analysis indicated that rGO had slightly higher crystallinity than TEGO, but both types of graphene based reinforcing agents also acted as nucleating agents during the integration of nanofiller in PA66 matrix by thermo-kinetic mixing. Both TEGO and rGO showed ease processing behavior with low viscosity profile compared to neat PA66's properties.

SEM images provided the differences of surfaces roughness by freeze-fracture surface analysis. To conclude, the results showed the importance of surface chemistry, dispersion state, and interfacial interactions between graphene and polymer matrix to attain an ideal composition for the fabrication of high performance PA66 nanocomposites with a scalable and fast production technique.

## ACKNOWLEDGMENTS

The authors would like to thank Kordsa Teknik Tekstil A.S. Company for providing financial support in our research activities.

## ORCID

Burcu Saner Okan  <https://orcid.org/0000-0002-5940-7345>

## REFERENCES

- [1] H. V. Madhad, D. V. Vasava, *J. Thermoplast. Compos. Mater.* **2019**, 1. <https://doi.org/10.1177/0892705719880942>.
- [2] X. Duan, B. Yu, T. Yang, Y. Wu, H. Yu, T. Huang, *J. Nanomater.* **2018**, 2018, 1.
- [3] Y. H. Kotp, *J. Water Process Eng.* **2019**, 30, 100553.
- [4] Y. Zhang, Y. Lu, X. J. Yan, W. S. Gao, H. Q. Chen, Q. Chen, Y. X. Bai, *Compos. Part A Appl. Sci. Manuf.* **2019**, 123, 149.
- [5] L. Qiu, Y. Chen, Y. Yang, L. Xu, X. Liu, *J. Nanomater.* **2013**, 2013, 8.
- [6] X. Liu, Q. Wu, *Macromol. Mater. Eng.* **2002**, 287, 180.
- [7] X. Fu, C. Yao, G. Yang, *RSC Adv.* **2015**, 5, 61688.
- [8] Y. H. Kotp, Y. A. Shebl, M. S. El-Deab, B. E. El-Anadouli, H. A. J. Shawky, *Inorg. Organomet. Polym. Mater.* **2017**, 27, 201.
- [9] Y. Chen, J. Gao, Q. Yan, X. Hou, S. Shu, M. Wu, N. Jiang, X. Li, J. Xu, C. Lin, J. Yu, *Veruscript Funct. Nanomater.* **2018**, 2, 1.
- [10] X. Wang, M. Song, *Nano Energy* **2013**, 2, 265.
- [11] H. Liu, L. Hou, W. Peng, Q. Zhang, X. J. Zhang, *Mater. Sci.* **2012**, 47, 8052.
- [12] H. Kim, A. A. Abdala, C. W. Macosko, *Macromolecules* **2010**, 43, 6515.
- [13] W. Gao, Y. Ma, Y. Zhang, Q. Chen, H. Chen, B. Zhu, J. Jia, A. Huang, K. Xie, Y. Bai, *Compos. Part A Appl. Sci. Manuf.* **2018**, 107, 479.
- [14] N. A. Kotov, *Nature* **2006**, 442, 254.
- [15] R. Verdejo, M. M. Bernal, L. J. Romasanta, M. A. Lopez-manchado, *J. Mater. Sci.* **2011**, 21, 3301.
- [16] S. Zhang, Y. Cheng, W. Xu, J. Li, J. Sun, J. Wang, C. Qin, L. Dai, *RSC Adv.* **2017**, 7, 56682.
- [17] E. L. Papadopoulou, F. Pignatelli, S. Marras, L. Marini, A. Davis, A. Athanassiou, I. S. Bayer, *RSC Adv.* **2016**, 6, 6823.
- [18] P. Mukhopadhyay, R. K. Gupta, *Graphite, Graphene, and their Polymer Nanocomposites*, CRC Press, Boca Raton **2012**.
- [19] N. Yesildag, C. Hopmann, M. Adamy, C. Windeck, *AIP Conf. Proc.* **2017**, 1914, 150001-1.
- [20] Z. Xu, C. Gao, *Macromolecules* **2010**, 43, 6716.
- [21] W. Hou, B. Tang, L. Lu, J. Sun, J. Wang, C. Qin, L. Dai, *RSC Adv.* **2014**, 4, 4848.
- [22] L. Gong, B. Yin, L. Li, M. Yang, *Compos. Part B* **2015**, 73, 49.
- [23] P. Steurer, R. Wissert, R. Thomann, R. Mülhaupt, *Macromol. Rapid Commun.* **2009**, 30, 316.
- [24] Y. Li, G. Yang, *Macromol. Rapid Commun.* **2004**, 25, 1714.
- [25] F. Chavarria, D. R. Paul, *Polymer* **2004**, 45, 8501.
- [26] D. C. Marcano, D. V. Kosynkin, J. M. Berlin, A. Sinitskii, Z. Sun, A. Slesarev, L. B. Alemany, W. Lu, J. M. Tour, *ACS Nano* **2010**, 4, 4806.
- [27] D. C. Marcano, D. V. Kosynkin, J. M. Berlin, A. Sinitskii, Z. Sun, A. S. Slesarev, L. B. Alemany, W. Lu, J. M. Tour, *ACS Nano* **2018**, 12, 2078.
- [28] X. Gao, J. Jang, S. Nagase, *J. Phys. Chem.* **2010**, 114, 832.
- [29] J. Seyyed Monfared Zanjani, B. Saner Okan, Y. Menciloglu, *Mater. Chem. Phys.* **2016**, 176, 58.
- [30] W. I. Hayes, P. Joseph, M. Z. Mughal, P. Papakonstantinou, *J. Solid State Electrochem.* **2014**, 19, 361.
- [31] A. O'Neill, D. Bakirtzis, D. Dixon, *Eur. Polym. J.* **2014**, 59, 353.
- [32] M. S. Dresselhaus, A. Jorio, M. Hofmann, G. Dresselhaus, R. Saito, *Nano Lett.* **2010**, 10, 751.
- [33] M. A. Pimenta, G. Dresselhaus, M. S. Dresselhaus, L. G. Cançado, A. Jorio, R. Saito, *Phys. Chem. Chem. Phys.* **2007**, 9, 1276.
- [34] S. Muralikrishna, K. Sureshkumar, T. S. Varley, D. H. Nagaraju, T. Ramakrishnappa, *Anal. Methods* **2014**, 6, 8698.
- [35] A. A. Vasileiou, M. Kontopoulou, A. Docoslis, *ACS Appl. Mater. Interfaces* **2014**, 6, 1916.
- [36] H. W. Ha, A. Choudhury, T. Kamal, D. Kim, S. Park, *ACS Appl. Mater. Interfaces* **2012**, 4, 4623.
- [37] J. S. M. Zanjani, L. H. Poudeh, B. G. Ozunlu, Y. E. Yagci, Y. Menciloglu, B. Saner Okan, *Polym. Int.* **2020**, 69, 771.
- [38] I. Alig, P. Pötschke, D. Lellinger, T. Skipa, S. Pegel, G. R. Kasaliwal, T. Villmow, *Polymer* **2012**, 53, 4.
- [39] V. Nagarajan, K. Zhang, M. Misra, A. K. Mohanty, *ACS Appl. Mater. Interfaces* **2015**, 7, 11203.
- [40] N. A. Jones, E. D. T. Atkins, M. J. Hill, *J. Polym. Sci. Part B Polym. Phys.* **2000**, 38, 1209.
- [41] J. Hendrix, R. Szeto, T. Nosker, J. Lynch-Branzoi, T. Emge, *Polymer* **2018**, 10, 1399.
- [42] M. Kyotani, S. Mitsuhashi, *J. Polym. Sci. Part A-2 Polym. Phys.* **1972**, 10, 1497.
- [43] F. Navarro-Pardo, G. Martínez-Barrera, A. Martínez-Hernández, V. Castaño, J. Rivera-Armenta, F. Medellín-Rodríguez, C. Velasco-Santos, *Materials* **2013**, 6, 3494.
- [44] N. Vasanthan, D. R. Salem, *J. Polym. Sci. Part B Polym. Phys.* **2000**, 38, 516.
- [45] M. M. Said, A. H. M. El-Aassar, Y. H. Kotp, H. A. Shawky, M. S. A. A. Mottaleb, *Desalin. Water Treat.* **2013**, 51, 4927.
- [46] L. Lim, I. J. Britt, M. A. Tung, *J. Appl. Polym. Sci.* **1999**, 71, 197.
- [47] D. M. Lincoln, R. A. Vaia, Z.-G. Wang, B. S. Hsiao, *Polymer* **2001**, 42, 1621.
- [48] X. Zhang, X. Fan, H. Li, C. Yan, *J. Mater. Chem.* **2012**, 22, 24081.
- [49] K. Q. Xiao, L. C. Zhang, I. Zarudi, *Compos. Sci. Technol.* **2007**, 67, 177.

- [50] T. D. Fornes, D. R. Paul, *Polymer* **2002**, *43*, 3247.
- [51] F. Du, R. C. Scogna, W. Zhou, S. Brand, J. E. Fischer, K. I. Winey, *Macromolecules* **2004**, *37*, 9048.

#### SUPPORTING INFORMATION

Additional supporting information may be found online in the Supporting Information section at the end of this article.

**How to cite this article:** Cakal Sarac E, Haghghi Poudeh L, Berktas I, Saner Okan B. Scalable fabrication of high-performance graphene/polyamide 66 nanocomposites with controllable surface chemistry by melt compounding. *J Appl Polym Sci.* 2020;e49972. <https://doi.org/10.1002/app.49972>